Evaluation of Ground Vehicle Protection Level Reduction due to Fusing GPS with Faulty Terrestrial Signals of Opportunity

Mu Jia, Joe Khalife, and Zaher M. Kassas
University of California, Irvine, USA

BIOGRAPHY

Mu Jia is a Ph.D. student at the University of California, Irvine and a member of the Autonomous Systems Perception, Intelligence, and Navigation (ASPIN) Laboratory. He received a B.E. in Vehicle Engineering from Shandong University, an M.E. in Mechanical Engineering from University of Defense Technology, and an M.S. in Mechanical Engineering from Duke University. His current research interests include autonomous ground vehicles, autonomous integrity monitoring, and opportunistic navigation.

Joe Khalife is a postdoctoral fellow at the University of California, Irvine and member of the Autonomous Systems Perception, Intelligence, and Navigation (ASPIN) Laboratory. He received a B.E. in Electrical Engineering, an M.S. in Computer Engineering from the Lebanese American University (LAU) and a Ph.D. in Electrical Engineering and Computer Science from the University of California, Irvine. From 2012 to 2015, he was a research assistant at LAU, and has been a member of the ASPIN Laboratory since 2015. He is a recipient of the 2016 IEEE/ION Position, Location, and Navigation Symposium (PLANS) Best Student Paper Award and the 2018 IEEE Walter Fried Award. His research interests include opportunistic navigation, autonomous vehicles, and software-defined radio.

Zaher (Zak) M. Kassas is an associate professor at the University of California, Irvine and director of the Autonomous Systems Perception, Intelligence, and Navigation (ASPIN) Laboratory. He received a B.E. in Electrical Engineering from the Lebanese American University, an M.S. in Electrical and Computer Engineering from The Ohio State University, and an M.S.E. in Aerospace Engineering and a Ph.D. in Electrical and Computer Engineering from The University of Texas at Austin. In 2018, he received the National Science Foundation (NSF) Faculty Early Career Development Program (CAREER) award, and in 2019, he received the Office of Naval Research (ONR) Young Investigator Program (YIP) award. He is a recipient of 2018 IEEE Walter Fried Award, 2018 Institute of Navigation (ION) Samuel Burka Award, and 2019 ION Col. Thomas Thurlow Award. His research interests include cyber-physical systems, estimation theory, navigation systems, autonomous vehicles, and intelligent transportation systems.

ABSTRACT

The protection level (PL) performance of an autonomous ground vehicle (AGV) due to fusing GPS signals with faulty terrestrial signals of opportunity (SOPs) is evaluated. The AGV is assumed to be equipped with receivers, which can produce a navigation solution from GPS and SOP pseudorange measurements. First, the effect of the number of SOPs on the PL reduction is analyzed. Then, the PL reduction under different assumptions of SOP fault probabilities is explored. The results show that while adding one SOP could increase the PL, adding two or more SOPs would significantly reduce the PLs. The results also demonstrate that even for highly unreliable SOPs (namely, those with fault probabilities as high as 10%), adding two or more SOPs would still reduce the PLs.

I. INTRODUCTION

The past few years have witnessed intense interest in pushing ground vehicles towards higher levels of automation, with the ultimate objective of achieving full autonomy, also known as Level 5 [1]. The potential impacts of deploying autonomous ground vehicles (AGVs) into our streets are promising, including reducing congestion and travel time and increased safety. However, there remains critical gaps between the capabilities of current technology and the stringent requirements of fully autonomous driving. Accurate, reliable, and resilient navigation is a key enabler of autonomous driving. Higher levels of automation not only rely on lane-level navigation accuracy, but also on tight protection levels (PLs) and integrity measures, especially on crowded urban roads, in which the AGV is surrounded by other vehicles, pedestrians, and bicyclists. Accurate navigation coupled with integrity monitoring (IM) are essential to guarantee the safety of the AGV itself, and most importantly the safety of humans in it and surrounding it. Virtually all current ground vehicles rely on global navigation satellite systems (GNSS) to estimate their position in a global frame. However, GNSS signals are jammable, spoofable, and may not be available

in deep urban canyons [2–4]. Recently, using signals of opportunity (SOPs) as a complement or an alternative to GNSS signals in GNSS-challenged environments has proven to improve the accuracy and integrity of the navigation solution [5]. However, SOPs are not designed for the safety-critical function of navigation; hence, their reliability as a navigation source is still under study. This paper addresses the following question: Could the navigation system integrity be improved by exploiting signals with unknown reliability? This paper answers this question by studying the effect of the number of SOPs and fault probabilities on IM performance.

Current ground vehicles are equipped with a suite of navigation sensors: GNSS receivers, vision-based sensors (red-green-blue (RGB) and infrared (IR) cameras), inertial navigation system (INS), and active range-finding sensors (lidar and radar). These sensors produce two categories of navigation functionality: (i) local navigation, which provides the position of the vehicle in a local coordinate system and (ii) global navigation, which provides the position of the vehicle in a global coordinate system. Over the past few decades, GNSS has monopolized global navigation. Future AGVs will require reliable lane-level-accurate navigation to travel safely, especially on urban roads. However, current GNSS technologies cannot sufficiently support the transition of ground vehicles from partial to full automation in terms of accuracy, integrity, and availability. For example, single point positioning (SPP), currently relied upon by ground and aerial vehicles, can only achieve meter-level accuracy [6]. Certain approaches, such as augmentation systems and real-time kinematic (RTK), could improve navigation accuracy and achieve sub-meter-level accuracy under certain conditions. However, these approaches cannot overcome the vulnerabilities of GNSS signals in deep urban canyons, where AGVs are expected to be ubiquitous.

Recent work have demonstrated how SOPs could improve navigation system accuracy in GNSS-challenged environments. SOPs (e.g. cellular signals [7–12], digital television signals [13–15], AM/FM radio signals [16–18], and low Earth orbit satellite (LEO) signals [19–24] have been exploited to produce navigation solutions in a standalone fashion or as an aiding source for an INS in the absence of GNSS signals [25]. For vehicular navigation, cellular signals are particularly attractive with their favorable characteristics, such as abundance in urban canyons, geometric and spectral diversity, high received power, and large bandwidth [26]. Cellular SOPs have been demonstrated to achieve meter-level accuracy for ground vehicles in a standalone fashion [27, 28] and when fused with an INS [29] and lane-level accuracy when fused with lidar [30].

Aside from accuracy, the trustworthiness of the navigation solution is another major concern in safety-critical applications, such as autonomous driving. The trustworthiness in the correctness of information by a positioning, navigation, and timing (PNT) system is measured as integrity. To improve the integrity of a navigation system, IM is usually used to detect anomalies or faults and to quantify the confidence of system integrity. There are two categories of IM frameworks, namely internal methods and external methods. External methods monitor the system's integrity by using external data sources such as ground-based augmentation system (GBAS) [31, 32] and satellite-based augmentation system (SBAS) [33]. In contrast, internal methods (e.g., receiver autonomous integrity monitoring (RAIM) and advanced RAIM (ARAIM)) leverage redundant measurements from existing signals [34, 35]. RAIM is a cost-effective technique for IM, since it does not require building additional infrastructure. Multi-constellation measurements [36] (e.g. Galileo, GLONASS, and Beidou) and aiding sensors (e.g., INS-GPS [37], lidar-GPS [6] and vision-GPS [38]) have been recently considered to improve the IM performance. In addition, several SOP-based IM studies have been conducted recently. In [39], cellular SOPs have been characterized and outlier detection and exclusion methods have been developed to deal with environment-induced faults, such as severe multipath conditions. In [40], a RAIM framework for ground vehicle navigation using cellular SOPs and an inertial measurement unit (IMU) was developed. GPS-SOP RAIM was proposed in [41] to support safe autonomous driving. GPS-SOP RAIM was also considered in [42] to improve the IM of unmanned aerial vehicles (UAVs).

While previous research have demonstrated that fusing cellular SOPs could improve the navigation accuracy and integrity, an open question remains unanswered: when does fusing SOPs benefit IM? While SOPs have favorable characteristics for enhancing the system integrity, the reliability of SOP transmitters has not been completely characterized and is very likely to be lower than that of GPS satellites, since the stakes of SOP transmitter faults are much lower than that of GPS satellite faults. This unknown reliability of SOPs compared to GPS satellites raises a question about the boundary condition under which incorporating SOPs in the navigation system can still improve the integrity of the system, particularly in terms of the number of available SOPs and their fault probability. This paper analyzes the PL reduction in different scenarios to answer the above question. This paper considers an AGV equipped with an SOP receiver that can produce pseudorange measurements from multiple terrestrial SOPs and a GPS receiver that can produce pseudorange measurements from multiple GPS satellites. The AGV produces a navigation solution from the SOP and GPS measurements. Moreover, the AGV performs IM using ARAIM aided by SOPs, which is referred to as ARAIM+SOP framework in this paper. This paper analyzes the performance of the ARAIM+SOP framework under different operation regimes through Monte Carlo numerical simulations. First, a simulator is constructed to characterize the influence of the number of SOPs on the horizontal PL (HPL) and vertical PL (VPL). Second, the PL reduction under different assumptions of SOP fault probabilities is analyzed.

The remainder of the paper is organized as follows. Section II. describes the measurement and SOP models employed in the paper. Section III. summarizes the ARAIM+SOP framework. Section IV. characterizes the PL reduction through Monte Carlo simulations. Concluding remarks are given in Section V.

II.   MODEL DESCRIPTION

This paper considers an AGV navigating in an environment that comprises N_{GPS} GPS satellites and N_{SOP} cellular transmitters. The cellular transmitters are stationary with known positions. The AGV is equipped with (i) a GPS receiver capable of producing pseudorange measurements from the N_{GPS} GPS satellites (e.g., [43–45]) and (ii) a receiver capable of producing pseudorange measurements from the N_{SOP} SOP transmitters (e.g., [8,9,27,46]). The AGV uses a weighted nonlinear least-squares (WNLS)-based estimator to compute the navigation solutions from the GPS and SOP pseudorange measurements and simultaneously performs IM and fault detection and exclusion (FDE). The IM algorithm, discussed in Section III, is based on the baseline ARAIM framework [34]. Although ARAIM handles multiple GNSS constellations, this paper considers only the GPS constellation. The proposed framework can be readily generalized to multiple GNSS constellations. The rest of this section presents the GPS and SOP pseudorange measurement models and the WNLS-based estimator used in the ARAIM+SOP framework, as well as the models of the GPS satellites and SOP transmitters' azimuth and elevation angles used to evaluate the ARAIM+SOP framework.

1.   GPS and SOP Pseudorange Measurement Models

a)   GPS Pseudorange Measurement Model

The m-th GPS pseudorange measurement after compensating for ionospheric delays, tropospheric delays, and the satellite's clock bias is modeled as:

$$z_{GPS_m}(k) = \|\boldsymbol{r}_r(k) - \boldsymbol{r}_{GPS_m}(k)\|_2 + c \cdot \delta t_{r,ck}(k) + v_{GPS_m}(k), \qquad k = 0, 1, \ldots, \quad m = 1, \ldots, N_{GPS}, \qquad (1)$$

where $z_{GPS_m}(k) = z'_{GPS_m}(k) - c \cdot \hat{\delta t}_{iono}(k) - c \cdot \hat{\delta t}_{tropo}(k) - c \cdot \hat{\delta t}_{GPS_m}(k)$; with $z'_{GPS_m}(k)$ being the uncompensated pseudorange; $\hat{\delta t}_{GPS_m}(k)$ is the estimated clock bias of the m-th GPS satellite; $\hat{\delta t}_{iono}(k)$ and $\hat{\delta t}_{tropo}(k)$ are the estimated ionospheric and tropospheric delays, respectively; c is the speed of light; $\boldsymbol{r}_r(k)$ and $\boldsymbol{r}_{GPS_m}(k)$ are the receiver and m-th satellite's three-dimensional (3-D) position vectors, respectively; $\delta t_{r,ck}(k)$ is the receiver's clock bias; and $v_{GPS_m}(k)$ denotes the measurement noise, which is modeled as a zero-mean Gaussian random sequence with a variance $\sigma^2_{GPS_m}$.

b)   SOP Pseudorange Measurement Model

The n-th SOP pseudorange measurement can be modeled as [47]

$$\bar{z}_{SOP_n}(k) = \|\boldsymbol{r}_r(k) - \boldsymbol{r}_{SOP_n}(k)\|_2 + c \cdot [\delta t_{r,ck}(k) - \delta t_{SOP_n}(k)] + \bar{v}_{SOP_n}(k), \qquad k = 0, 1, \ldots, \quad n = 1, \ldots, N_{SOP}, \quad (2)$$

where $\boldsymbol{r}_{SOP_n}(k)$ and $\delta t_{SOP_n}(k)$ are the position and clock bias of the n-th SOP transmitter, respectively; and $\bar{v}_{SOP_n}$ is the SOP measurement noise, which is modeled as a zero-mean Gaussian random sequence with a variance σ^2_{user,SOP_n}. The model for σ^2_{user,SOP_n} is given in Subsection III.1. It was noted in [48] that the difference $c \cdot [\delta t_{r,ck}(k) - \delta t_{SOP_n}(k)]$ can be modeled as

$$c \cdot [\delta t_{r,ck}(k) - \delta t_{SOP_n}(k)] = c\delta t_{r,SOP}(k) + c\delta t_{SOP_n,0} + \epsilon_n(k), \qquad k = 0, 1, \ldots, \quad n = 1, \ldots, N_{SOP}, \qquad (3)$$

where $c\delta t_{r,SOP}(k)$ is a common term driving the difference between the receiver and SOP clock biases, $c\delta t_{SOP_n,0}$ is an initial bias, and $\epsilon_n(k)$ is an error term modeled as a zero-mean Gaussian random variable with variance $\sigma^2_{\epsilon_n}$. The value of $\sigma^2_{\epsilon_n}$ is discussed in Subsection III.1. It is assumed that the initial biases $\{c\delta t_{SOP_n,0}\}_{n=1}^{N_{SOP}}$ were calibrated prior to IM. Finally, after initial bias calibration, the n-th SOP pseudorange measurement z_{SOP_n} can be expressed as

$$z_{SOP_n} = \|\boldsymbol{r}_r(k) - \boldsymbol{r}_{SOP_n}(k)\|_2 + c\delta t_{r,SOP}(k) + v_{SOP_n}(k), \qquad k = 0, 1, \ldots, \quad n = 1, \ldots, N_{SOP}, \qquad (4)$$

where $v_{SOP_n}(k) \triangleq \epsilon_n(k) + \bar{v}_{SOP_n}(k)$.

2.   Navigation Solution

The AGV aims to estimate its position vector using GPS and SOP pseudorange measurements using a WNLS. To this end, the GPS and SOP receivers' clock biases must be estimated alongside the AGV's position to avoid biasing the navigation solution. The vector to be estimated is given by

$$\boldsymbol{x}(k) \triangleq \left[\boldsymbol{r}_r{}^\mathsf{T}(k), c\delta t_{r,ck}(k), c\delta t_{r,SOP}(k)\right]^\mathsf{T}.$$

The time argument is omitted in the following for compactness of notation. The all-in-view combined GPS-SOP measurement vector can be formed according to

$$\boldsymbol{z} \triangleq \left[z_{GPS_1}, \ldots, z_{GPS_{N_{GPS}}}, z_{SOP_1}, \ldots, z_{SOP_{N_{SOP}}} \right]^{\mathsf{T}}.$$

A WNLS is then iterated to obtain an estimate of $\boldsymbol{x}$, denoted by $\hat{\boldsymbol{x}}$, using $\boldsymbol{z}$. Let l denote the iteration number, $\hat{\boldsymbol{x}}_l$ the estimate at iteration l, and $\hat{\boldsymbol{z}}_l$ the measurement prediction calculated using $\hat{\boldsymbol{x}}_l$. The all-in-view navigation solution update is obtained from the normal equations according to

$$\Delta \boldsymbol{x}_l = \left(\mathbf{H}_l^{\mathsf{T}} \mathbf{W} \mathbf{H}_l \right)^{-1} \mathbf{H}_l^{\mathsf{T}} \mathbf{W} \left(\boldsymbol{z} - \hat{\boldsymbol{z}}_l \right), \tag{5}$$

where $\mathbf{H}_l$ is the measurement Jacobian evaluated at $\hat{\boldsymbol{x}}_l$ and $\mathbf{W}$ is the weight matrix given by $\mathbf{W} = \mathbf{C}_{int}^{-1}$, where $\mathbf{C}_{int}$ is a diagonal matrix whose diagonal elements $\{\mathbf{C}_{int}(j,j)\}_{j=1}^{N_{GPS}+N_{SOP}}$ are the measurement noise variances used for integrity. The values of the diagonal elements of $\mathbf{C}_{int}$ are discussed in Subsection III.3. The WNLS estimate at the $(l+1)$-th iteration is updated according to

$$\hat{\boldsymbol{x}}_{l+1} = \hat{\boldsymbol{x}}_l + \Delta \boldsymbol{x}_l,$$

and the iteration number is subsequently increased according to $l \leftarrow l+1$. After convergence, the all-in-view navigation solution is denoted $\hat{\boldsymbol{x}}^{(0)}$, the measurement prediction after convergence is denoted $\hat{\boldsymbol{z}}^{(0)}$, and the residual at convergence is denoted $\boldsymbol{y}$, which is given by

$$\boldsymbol{y} \triangleq \boldsymbol{z} - \hat{\boldsymbol{z}}^{(0)}.$$

Let $\mathbf{H}$ denote the measurement Jacobian after convergence, which can be parameterized by the GPS satellites' and SOP transmitters' azimuth and elevation angles according to

$$\mathbf{H} = \left[\begin{array}{c} \mathbf{H}_{GPS} \\ \mathbf{H}_{SOP} \end{array} \right], \tag{6}$$

where

$$\mathbf{H}_{GPS} \triangleq \left[\begin{array}{ccccc} -\cos(el_{GPS_1})\sin(az_{GPS_1}) & -\cos(el_{GPS_1})\cos(az_{GPS_1}) & -\sin(el_{GPS_1}) & 1 & 0 \\ \vdots & \vdots & \vdots & \vdots & \vdots \\ -\cos(el_{GPS_{N_{GPS}}})\sin(az_{GPS_{N_{GPS}}}) & -\cos(el_{GPS_{N_{GPS}}})\cos(az_{GPS_{N_{GPS}}}) & -\sin(el_{GPS_{N_{GPS}}}) & 1 & 0 \end{array} \right],$$

$$\mathbf{H}_{SOP} \triangleq \left[\begin{array}{ccccc} -\cos(el_{SOP_1})\sin(az_{SOP_1}) & -\cos(el_{SOP_1})\cos(az_{SOP_1}) & -\sin(el_{SOP_1}) & 0 & 1 \\ \vdots & \vdots & \vdots & \vdots & \vdots \\ -\cos(el_{SOP_{N_{SOP}}})\sin(az_{SOP_{N_{SOP}}}) & -\cos(el_{SOP_{N_{SOP}}})\cos(az_{SOP_{N_{SOP}}}) & -\sin(el_{SOP_{N_{SOP}}}) & 0 & 1 \end{array} \right],$$

where az_{GPS_m} and el_{GPS_m} are the m-th GPS satellite's azimuth and elevation angles, respectively, and az_{SOP_n} and el_{SOP_n} are the n-th SOP's azimuth and elevation angles, respectively.

3. GPS Satellite Azimuth and Elevation Angle Characterization

As it can be seen from the expression of $\mathbf{H}$ in (6), the GPS satellites' and SOP transmitters' azimuth and elevation angles are enough to characterize the geometry between the AGV and the navigation sources. This paper assumes a stationary receiver located in Orange County, California, USA. The receiver position is fixed at $\boldsymbol{r}_r \equiv 10^6 \times [-2, 482345, -4, 700049, 3.513616]^{\mathsf{T}}$ expressed in the Earth-Centered-Earth-Fixed (ECEF) frame. The azimuth and elevation angles of all visible satellites at that location and at any point in time can be readily calculated. Since the nominal orbital period of a GPS satellites is 11 hours 58 minutes, which is almost exactly half of a sidereal day, the same exact GPS satellite configuration will repeat itself above the specified location after one full day on Earth [49]. As such, to obtain a realization of GPS azimuth and elevation angles, a random time is chosen from a 24-hour interval at which the satellite positions are determined. Subsequently, the azimuth and elevation angles are calculated and only GPS satellites above an elevation angle mask $el_{mask} = 5°$ are retained.

4. SOP Azimuth and Elevation Angle Models

The cellular SOP network is modeled as a binomial point process (BPP), where the horizontal positions of N SOPs are independently and uniformly distributed over an annular region centered at the receiver, i.e., $\mathbb{B}_r(d_{SOP_{min}}, d_{SOP_{max}}) = \pi(d_{SOP_{max}}^2 - d_{SOP_{min}}^2)$ [50], where $d_{SOP_{min}}$ is the minimum horizontal distance required for the far-field assumption to

hold and $d_{SOP_{\max}}$ is the maximum horizontal distance for which ranging signals can be detected by the receiver (see Figure 1(a) for $N = 15$). The altitudes of the SOPs relative to the receiver are assumed to be uniformly distributed between $h_{SOP_{\min}}$ and $h_{SOP_{\max}}$. As shown in Figure 1(b), the location of the n-th SOP is represented by $(d_{SOP_n}, h_{SOP_n}, az_{SOP_n})$, where d_{SOP_n} and h_{SOP_n} are the horizontal and vertical distances between the n-th SOP and the receiver, respectively. As a result, the elevation angle of the n-th SOP and the range to the n-th SOP r_{SOP_n} can be calculated as

$$el_{SOP_n} = \tan^{-1}\left(\frac{h_{SOP_n}}{d_{SOP_n}}\right), \qquad r_{SOP_n} = \sqrt{d_{SOP_n}^2 + h_{SOP_n}^2}.$$
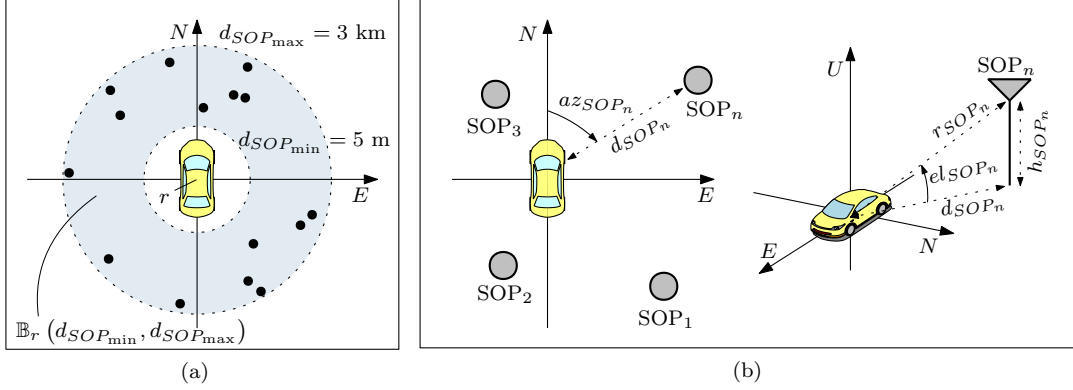
Figure 1: (a) BPP realization with $N = 15$, SOP transmitters uniformly lie in the annular region. (b) Parametrization of the n-th SOP position by its range r_{SOP_n}, azimuth angle az_{SOP_n} and elevation angle el_{SOP_n}.

III.   ARAIM+SOP FRAMEWORK

This section introduces the ARAIM+SOP framework adopted by this paper to perform IM. ARAIM+SOP is developed based on the baseline multiple hypothesis solution separation (MHSS) ARAIM introduced in [34]. The MHSS ARAIM framework is capable of incorporating different navigation signals with different signal properties, e.g., different error variance, maximum nominal biases, and probability of single or constellation faults. The ARAIM+SOP framework utilizes this flexibility of multiple-source ARAIM to incorporate SOPs as a navigation constellation. While multiple GNSS constellations can be handled by the ARAIM+SOP framework, this paper considers GPS-SOP ARAIM as an initial study. The ARAIM+SOP framework is readily extendable to multiple GNSS constellations. Table 1 summarizes the inputs for the ARAIM+SOP algorithm.

The ARAIM+SOP algorithm first determines the fault modes to be monitored based on the Integrity Support Message (ISM) and SOP signal error characterization obtained from experimental campaigns. The prior probabilities of the fault modes are also computed in this step. During IM, the ARAIM+SOP conducts solution separation tests to detect and exclude potential faults in the system. The ARAIM+SOP framework also includes a chi-squared test which serves as a sanity check for potential faults outside the fault modes obtained by the algorithm. A brief description of the ARAIM+SOP is provided by the following sections. Detailed descriptions can be found in [34].

1.   SOP Integrity Parameters

In order to perform IM with SOP pseudoranges, their integrity parameters must be known, mainly $\{\sigma_{URA,SOP_n}\}_{n=1}^{N_{SOP}}$, $\{\sigma_{URE,SOP_n}\}_{n=1}^{N_{SOP}}$, $\{b_{nom,SOP_n}\}_{n=1}^{N_{SOP}}$, $\{P_{SOP_n}\}_{n=1}^{N_{SOP}}$, and $P_{const,SOP}$. The performance of the ARAIM+SOP framework is characterized for various values of N_{SOP} and $\{P_{SOP_n}\}_{n=1}^{N_{SOP}}$. Moreover, this paper will not consider GPS or SOP constellation faults, as the probability of either to happen is assumed to be extremely low. Therefore, $P_{const,GPS}$ and $P_{const,SOP}$ are set to be 0. The rest of the SOP integrity parameters are discussed below.

a)   SOP User Range Accuracy (URA) Standard Deviation

Figure 2(a) shows experimentally recorded data corresponding to a realization of $c \cdot [\delta t_{r,GPS}(k) - \delta t_{SOP_n}(k)]$ for three SOPs, after initial bias calibration, over a period of 24 hours. It can be clearly seen from Figure 2(a) that $\{c \cdot [\delta t_{r,GPS}(k) - \delta t_{SOP_n}(k)]\}_{n=1}^{3}$ are driven by a common term, justifying the right hand side of (3). Figure 2(b) shows the resulting $\epsilon_n(k)$, representing the deviation of $c \cdot [\delta t_{r,GPS}(k) - \delta t_{SOP_n}(k)]$ from the common term, for the realization in Figure 2(a). Figure 2(b) shows that $\{\epsilon_n\}_{n=1}^{3}$ can be considered as noise terms. Assuming ergodicity, the values of $\{\sigma_{\epsilon_n}\}_{n=1}^{3}$ range from 0.6 to 0.73 m. Therefore, σ_{URA,SOP_n} is chosen to be 1 m for all n, to guarantee that $\sigma_{\epsilon_n} \leq \sigma_{URA,SOP_n}$.

Table 1: Inputs to the ARAIM+SOP Algorithm

Input	Description	Obtained from
$\{z_{GPS_m}\}_{m=1}^{N_{GPS}}$	Pseudorange for m-th GPS satellite after dual frequency correction, tropospheric correction, and smoothing are performed	Receiver
$\{z_{SOP_n}\}_{n=1}^{N_{SOP}}$	Pseudorange for n-th SOP	Receiver
$\{\sigma_{URA,GPS_m}\}_{m=1}^{N_{GPS}}$	Standard deviation of the clock and ephemeris error of m-th satellite used for integrity	ISM
$\{\sigma_{URE,GPS_m}\}_{m=1}^{N_{GPS}}$	Standard deviation of the clock and ephemeris error of m-th satellite used for accuracy and continuity	ISM
$\{\sigma_{URA,SOP_n}\}_{n=1}^{N_{SOP}}$	Standard deviation of the clock error of n-th SOP used for integrity	Discussed in Subsection III.1
$\{\sigma_{URE,SOP_n}\}_{n=1}^{N_{SOP}}$	Standard deviation of the clock error of n-th SOP used for accuracy and continuity	Discussed in Subsection III.1
$\{b_{nom,GPS_m}\}_{m=1}^{N_{GPS}}$	Maximum nominal bias for GPS used for integrity	ISM
$\{b_{nom,SOP_n}\}_{n=1}^{N_{SOP}}$	Maximum nominal bias for SOP used for integrity	Discussed in Subsection III.1
$\{P_{GPS_m}\}_{m=1}^{N_{GPS}}$	Probability of a single GPS fault	ISM
$\{P_{SOP_n}\}_{n=1}^{N_{SOP}}$	Probability of a single SOP fault	Varied
$P_{const,GPS}$	Probability of GPS constellation fault	0
$P_{const,SOP}$	Probability of SOP constellation fault	0
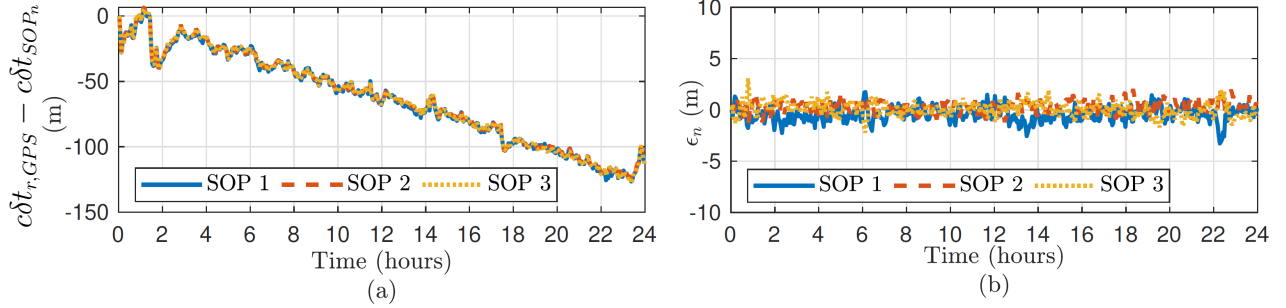
Figure 2: (a) Experimentally recorded data corresponding to a realization of $c \cdot [\delta t_r(k) - \delta t_{SOP_n}(k)]$ for three SOPs, after initial bias calibration, over a period of 24 hours. (b) Resulting $\epsilon_n(k)$ for the three SOPs in (a).

b) SOP User Range Error (URE) Standard Deviation

In GPS, it is usually assumed

$$\sigma_{URE,GPS} = \frac{2}{3}\sigma_{URA,GPS}.$$

This relationship is also used for $\sigma_{URE,SOP}$ and $\sigma_{URA,SOP}$.

c) SOP Maximum Nominal Bias

The maximum nominal bias typically used in GPS ARAIM applications is around 1 m. Due to the difference in the propagation channels, the SOP maximum nominal bias is taken to be threefold that of GPS; hence, b_{nom,SOP_n} is chosen to be 3 m for all n.

2. Determination of Fault Modes to be Monitored

The first step of the ARAIM+SOP framework is to determine the fault modes to be monitored and calculate their prior probabilities. The objective of this step is to choose the smallest subset of all the possible fault modes and make sure that the sum of the probabilities of the modes that are not monitored do not exceed a predefined threshold P_{THRES}. The algorithm moves the fault modes from the list of not monitored to the monitored list until the total probability of the remaining modes' occurrence is under P_{THRES}. The fault modes are selected from the fault modes with smaller number of faulty satellites (which is defined as the degree of the fault modes) to fault modes with larger degrees. Note that the maximum number of simultaneous faults is determined by the probability of single transmitter fault, constellation fault probability, and P_{THRES}.

After the $N_{faultmodes}$ fault modes are determined, the prior probability of each fault mode $P_{fault}^{(i)}$ is calculated based on the probability of single transmitter fault and constellation fault of GPS and SOP.

3. Covariance Matrix For Integrity

The ARAIM+SOP framework computes the pseudorange error diagonal covariance matrices $\mathbf{C}_{int,GPS}$ (used for integrity) and $\mathbf{C}_{acc,GPS}$ (used for accuracy and continuity) using the equation given by [34]:

$$\mathbf{C}_{int,GPS}(m, m) = \sigma_{URA,GPS_m}^2 + \sigma_{user,GPS_m}^2$$

$$\mathbf{C}_{acc,GPS}(m, m) = \sigma_{URE,GPS_m}^2 + \sigma_{user,GPS_m}^2,$$

where σ_{user,GPS_m} is the standard deviation of the GPS code noise and multipath error, which is calculated as

$$\sigma_{user,GPS_m} = \sqrt{\frac{f_{L1}^4 + f_{L5}^4}{(f_{L1}^2 - f_{L5}^2)^2}} \sqrt{\sigma_{MP}^2 + \sigma_{Noise}^2},$$

where f_{L1} and f_{L5} are the L1 an L5 frequency of GPS signal, $\sigma_{MP} = 0.13 + 0.53 \cdot \exp(-el_{GPS_m}/6.9)$ and $\sigma_{MP} = 0.15 + 0.43 \cdot \exp(-el_{GPS_m}/6.9)$.

Similarly, the SOP pseudorange error diagonal covariance matrices are given by

$$\mathbf{C}_{int,SOP}(n, n) = \sigma_{URA,SOP_n}^2 + \sigma_{user,SOP_n}^2$$

$$\mathbf{C}_{acc,SOP}(n, n) = \sigma_{URE,SOP_n}^2 + \sigma_{user,SOP_n}^2,$$

where σ_{user,SOP_m} is the standard deviation of the SOP multipath error which can be calculated as a function of the distance between the receiver and the SOP transmitter. The equation for σ_{user,SOP_m} is given in [50] (cf. (10)).

The pseudorange error diagonal covariance matrices for the overall system are given by

$$\mathbf{C}_{int} = \text{blkdiag}\left[\mathbf{C}_{int,GPS}, \mathbf{C}_{int,SOP}\right]$$

$$\mathbf{C}_{acc} = \text{blkdiag}\left[\mathbf{C}_{acc,GPS}, \mathbf{C}_{acc,SOP}\right],$$

where blkdiag donates block diagonal matrix.

4. Solution Separation Test

The ARAIM+SOP conducts multiple hypothesis testing to detect and locate the faults. Each fault mode determined by the previous step corresponds to one hypothesis. For each alternative hypothesis, a fault-tolerant solution is defined as the navigation solution obtained from measurements excluding the hypothesized faulty measurements in the corresponding fault mode. The difference between the fault-tolerant solutions and the all-in-view solution serves as the test statistics for each alternative hypothesis. The difference vector for the i-th fault mode is computed as

$$\Delta\hat{\boldsymbol{x}}^{(i)} = \hat{\boldsymbol{x}}^{(i)} - \hat{\boldsymbol{x}}^{(0)} = (\mathbf{S}^{(i)} - \mathbf{S}^{(0)})\boldsymbol{y}, \tag{7}$$

where $\hat{\boldsymbol{x}}^{(i)}$ and $\hat{\boldsymbol{x}}^{(0)}$ are the i-th fault-tolerant solution and the all-in-view solution, respectively; $\boldsymbol{y}$ is the residual vector from the all-in-view solution; and

$$\mathbf{S}^{(i)} \triangleq (\mathbf{H}^\mathsf{T}\mathbf{W}^{(i)}\mathbf{H})^{-1}\mathbf{H}^\mathsf{T}\mathbf{W}^{(i)}, \tag{8}$$

where $\mathbf{W}^{(i)}$ is the diagonal weighing matrix, which is defined as

$$\mathbf{W}^{(i)}(j, j) = \begin{cases} \mathbf{C}_{int}^{-1}(j, j) & \text{if measurement } j \text{ is hypothesized faulty,} \\ 0 & \text{otherwise.} \end{cases}$$

The test threshold for the q-th coordinate ($q = 1, 2, $ or 3) of fault mode i is denoted by $T_{i,q}$. The thresholds can be computed from the variance of $\Delta\hat{\boldsymbol{x}}^{(i)}$ and the continuity budget. For each i and q, the solution separation test is

$$|\hat{x}_q^{(i)} - \hat{x}_q^{(0)}| \overset{?}{\lessgtr} T_{i,q}. \tag{9}$$

If the test fails for any i and q, the algorithm will try to perform fault exclusion.

5. Chi-squared Test

Other than the solution separation tests, the ARAIM-SOP framework conducts a chi-squared test as a sanity check for faults outside of the fault modes monitored in the framework. The chi-squared statistic is an upper bound of all solution separation test, i.e., the detectable faults will manifest themselves in this test statistic [34].

6. Protection Level Calculation

After all the fault detection and exclusion is performed, the HPL can be calculated. The algorithm first computes HPL_q for the two horizontal directions, i.e., $q \equiv 1, 2$, from the well-established equation [34]

$$
\begin{aligned}
2Q\left(\frac{HPL_q - b_q^{(0)}}{\sigma_q^{(0)}}\right) + \sum_{i=1}^{N_{fault,modes}} P_{fault}^{(i)} Q\left(\frac{HPL_q - T_{k,i} - b_q^{(i)}}{\sigma_q^{(i)}}\right) = \\
\frac{1}{2}PHMI_{HOR}\left(1 - \frac{P_{fault,notmonitored}}{PHMI_{VERT} + PHMI_{HOR}}\right),
\end{aligned}
\tag{10}
$$

where Q is the tail distribution function of the standard Gaussian distribution; $b_q^{(i)}$ is the worst case impact of the nominal bias in the q direction; $\sigma_q^{(i)}$ is the variance of the fault-tolerant position estimate; $P_{fault}^{(i)}$ is the probability of fault mode i; $P_{fault,notmonitored}$ is the probability of the faults that are not included in the fault modes; and $PHMI_{VERT}$ and $PHMI_{HOR}$ are the integrity budget for the vertical and horizontal components, respectively. The HPL is further given by

$$
HPL = \sqrt{HPL_1^2 + HPL_2^2}.
\tag{11}
$$

The VPL can be calculated from an equation similar to equation (10), except that $q \equiv 3$.

## IV. PROTECTION LEVEL REDUCTION CHARACTERIZATION

Monte Carlo simulations are conducted to characterize the PL in different scenarios. In each simulation, it is assumed that there are 6 GPS satellites available above the elevation mask $el_{mask} = 5°$. The GPS satellite positions are randomly drawn as discussed in Subsection II.3. Cellular base stations are placed randomly based on the BPP model mentioned in Subsection II.4. The vertical distances between the user receiver and the SOP transmission antenna are assumed to be uniformly distributed between 5 m to 25 m, i.e., $h_{SOP_n} \sim \mathcal{U}(5, 25)$ for $n = 1, \ldots, N_{SOP}$. The SOP elevation angles $el_{SOP,n}$ and pseudorange noise standard deviations σ_{user,SOP_n} are calculated according to h_{SOP_n}, d_{SOP_n}, and az_{SOP_n}. The simulation settings are tabulated in Table 2.

Table 2: SIMULATION SETTINGS

Parameter	Definition	Value
N_{GPS}	Number of available GPS satellites included in the navigation solution	6
N_{SOP}	Number of SOP transmitters included in the navigation solution	0 to 7
$PHMI_{HOR}$	Integrity budget for the horizontal component	10^{-7}
$PHMI_{VERT}$	Integrity budget for the vertical component	10^{-9}
PFA_{HOR}	Continuity budget allocated to the horizontal component	10^{-7}
PFA_{VERT}	Continuity budget allocated to the vertical component	10^{-9}
$\{\sigma_{URA,GPS_m}\}_{m=1}^{N_{GPS}}$	Standard deviation of the clock and ephemeris error of satellite m used for integrity	1 m
$\{\sigma_{URA,SOP_n}\}_{n=1}^{N_{SOP}}$	Standard deviation of the clock error of SOP n used for integrity	1 m

1. Evaluating Number of SOPs

The first study is to characterize the effect of the number of SOPs on the PL reduction. The VPL and HPL are first computed with the GPS measurements only. Then, the number of SOP transmitters was varied as $N_{SOP} \in \{1, \ldots, 7\}$. For each N_{SOP}, 10^5 realizations are drawn to compute the average PL reductions from GPS-only solutions to GPS-SOP solutions. The SOP fault probability was set to 10^{-4}. The results are shown in Figure 3.
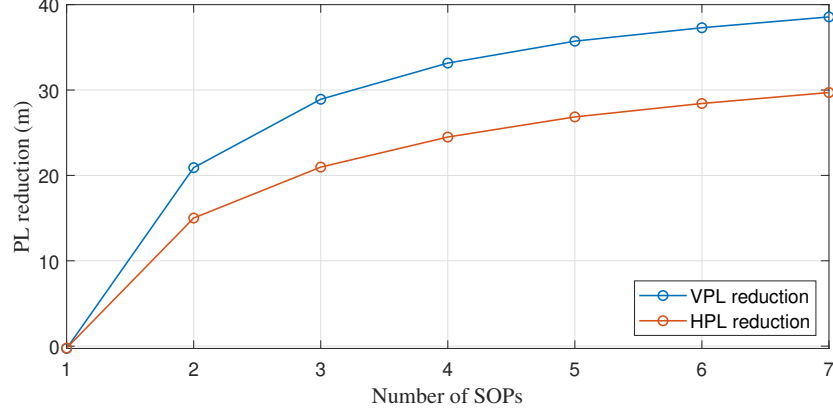
Figure 3: The average reduction in VPL and HPL after adding different number of SOP measurements. Each data point is obtained by averaging over 10^5 Monte Carlo realizations.

The following may be concluded from Figure 3. The number of SOP measurements plays an important role in PL reduction. Surprisingly, incorporating one SOP measurement in the framework *degrades* the IM performance. This is likely because the probability of single SOP transmitter fault is higher than that of GPS. The increased redundancy is not enough to compensate for the effects of increased probability of fault and larger number of fault modes. Furthermore, adding two or more SOPs will improve the IM performance significantly under the assumption of SOP fault probability being 10^{-4}. The PL reduction does not vary by much as N_{SOP} exceeds 5.

2. Evaluating Probability of Faults

As the probability of SOP fault has not been thoroughly characterized, it is essential to evaluate the performance of the ARAIM+SOP framework under different probability of fault assumptions. In these simulations, the probability of single SOP fault P_{SOP_n} is swept from 10^{-5} to 10^{-1}. The SOP measurement is considered to be faulty when multipath or non-line-of-sight (NLOS) conditions cause unmodeled biases or the SOP transmitter encounters anomalies which induce errors in the estimated position. The lower bound of P_{SOP_n} is chosen based on the assumption that the SOP measurements are less reliable than GPS measurements. It is also worth noting that P_{SOP_n} is not likely to be as high as 10^{-1}. However, 10^{-1} is chosen as an extreme case to study the performance in extreme regimes. For each N_{SOP} and P_{SOP_n} pair, 10^5 realizations are drawn to compute the average PL reduction. The results are shown in Figure 4.

The following conclusions may be drawn from Figure 4. Generally, the PL reduction will decrease with the probability of SOP transmitter fault increasing. However, in reasonable fault probability ranges (10^{-5} to 10^{-3}), the IM performance is more sensitive to the number of SOPs than the probability of fault. With enough SOP transmitters available, the less reliable SOP measurements (with P_{SOP_n} up to 10^{-3}) can still reduce the PLs significantly. Although less significant, PL reductions can still be achieved with high probability of SOP fault. It is worth re-iterating that these scenarios are not likely to happen in real life.

V. CONCLUSION

The performance of ARAIM+SOP was characterized by Monte Carlo numerical simulations. The paper analyzed the effect of the number of SOPs and the SOPs' fault probabilities on PL reduction. The following conclusions can be drawn from these analyses. First, the number of SOPs affects the PLs of the ARAIM+SOP framework significantly. Adding only one SOP could degrade the IM perofrmance. However, adding two or more SOPs will significantly improve the performance, and this improvement significantly grows up until about 5 SOPs. Beyond 5 SOPs, the improvement does not vary by much. Second, while incorporating a single faulty SOP does not benefit PL reduction, incorporating multiple highly unreliable SOPs will reduce the PL.
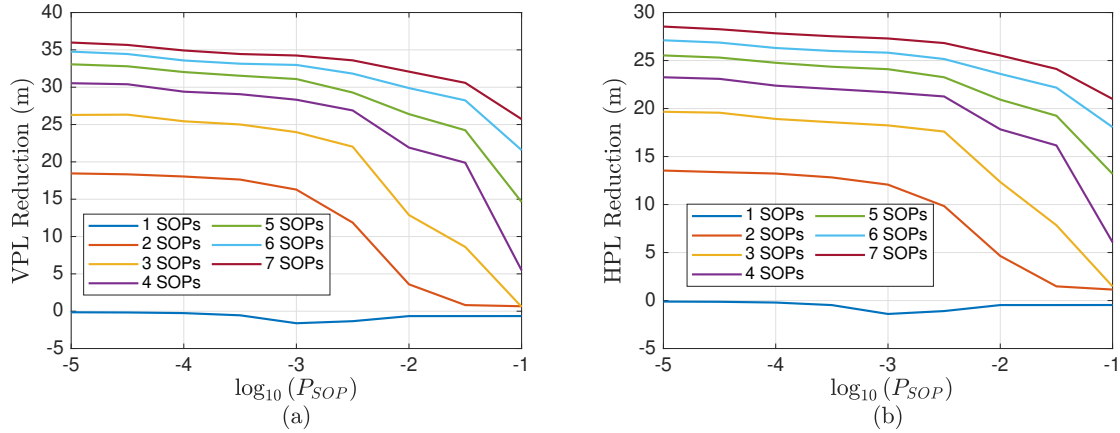
Figure 4: The reduction in VPL and HPL for adding different number of SOPs with different probability of SOP fault. (a) VPL reduction. (b) HPL reduction.

REFERENCES

[1] SAE International, "Taxonomy and definitions for terms related to driving automation systems for on-road motor vehicles," Tech. Rep., June 2018.

[2] R. Ioannides, T. Pany, and G. Gibbons, "Known vulnerabilities of global navigation satellite systems, status, and potential mitigation techniques," *Proceedings of the IEEE*, vol. 104, no. 6, pp. 1174–1194, February 2016.

[3] D. Borio, F. Dovis, H. Kuusniemi, and L. Presti, "Impact and detection of GNSS jammers on consumer grade satellite navigation receivers," *Proceedings of the IEEE*, vol. 104, no. 6, pp. 1233–1245, February 2016.

[4] N. Zhu, J. Marais, D. Betaille, and M. Berbineau, "GNSS position integrity in urban environments: A review of literature," *IEEE Transactions on Intelligent Transportation Systems*, vol. 19, no. 9, pp. 2762–2778, September 2018.

[5] Z. Kassas, J. Khalife, A. Abdallah, and C. Lee, "I am not afraid of the jammer: navigating with signals of opportunity in GPS-denied environments," in *Proceedings of ION GNSS Conference*, 2020, pp. 1566–1585.

[6] D. Imparato, A. El-Mowafy, and C. Rizos, "Integrity monitoring: From airborne to land applications," in *Multifunctional Operation and Application of GPS*. IntechOpen, 2018, pp. 23–43.

[7] C. Gentner, T. Jost, W. Wang, S. Zhang, A. Dammann, and U. Fiebig, "Multipath assisted positioning with simultaneous localization and mapping," *IEEE Transactions on Wireless Communications*, vol. 15, no. 9, pp. 6104–6117, September 2016.

[8] M. Driusso, C. Marshall, M. Sabathy, F. Knutti, H. Mathis, and F. Babich, "Vehicular position tracking using LTE signals," *IEEE Transactions on Vehicular Technology*, vol. 66, no. 4, pp. 3376–3391, April 2017.

[9] K. Shamaei, J. Khalife, and Z. Kassas, "Exploiting LTE signals for navigation: Theory to implementation," *IEEE Transactions on Wireless Communications*, vol. 17, no. 4, pp. 2173–2189, April 2018.

[10] J. Khalife and Z. Kassas, "Navigation with cellular CDMA signals – part II: Performance analysis and experimental results," *IEEE Transactions on Signal Processing*, vol. 66, no. 8, pp. 2204–2218, April 2018.

[11] J. del Peral-Rosado, J. López-Salcedo, F. Zanier, and G. Seco-Granados, "Position accuracy of joint time-delay and channel estimators in LTE networks," *IEEE Access*, vol. 6, no. 25185–25199, p. April, 2018.

[12] Z. Kassas, A. Abdallah, and M. Orabi, "Carpe signum: seize the signal – opportunistic navigation with 5G," *Inside GNSS Magazine*, vol. 16, no. 1, pp. 52–57, 2021.

[13] P. Thevenon, S. Damien, O. Julien, C. Macabiau, M. Bousquet, L. Ries, and S. Corazza, "Positioning using mobile TV based on the DVB-SH standard," *NAVIGATION, Journal of the Institute of Navigation*, vol. 58, no. 2, pp. 71–90, 2011.

[14] C. Yang, T. Nguyen, and E. Blasch, "Mobile positioning via fusion of mixed signals of opportunity," *IEEE Aerospace and Electronic Systems Magazine*, vol. 29, no. 4, pp. 34–46, April 2014.

[15] L. Chen, O. Julien, P. Thevenon, D. Serant, A. Pena, and H. Kuusniemi, "TOA estimation for positioning with DVB-T signals in outdoor static tests," *IEEE Transactions on Broadcasting*, vol. 61, no. 4, pp. 625–638, 2015.

[16] S. Fang, J. Chen, H. Huang, and T. Lin, "Is FM a RF-based positioning solution in a metropolitan-scale environment? A probabilistic approach with radio measurements analysis," *IEEE Transactions on Broadcasting*, vol. 55, no. 3, pp. 577–588, September 2009.

[17] A. Popleteev, "Indoor positioning using FM radio signals," Ph.D. dissertation, University of Trento, Italy, 2011.

[18] V. Moghtadaiee and A. Dempster, "Indoor location fingerprinting using FM radio signals," *IEEE Transactions on Broadcasting*, vol. 60, no. 2, pp. 336–346, June 2014.

[19] R. Landry, A. Nguyen, H. Rasaee, A. Amrhar, X. Fang, and H. Benzerrouk, "Iridium Next LEO satellites as an alternative PNT in GNSS denied environments–part 1," *Inside GNSS Magazine*, pp. 56–64., May 2019.

[20] Z. Tan, H. Qin, L. Cong, and C. Zhao, "New method for positioning using IRIDIUM satellite signals of opportunity," *IEEE Access*, vol. 7, pp. 83 412–83 423, 2019.

[21] Z. Kassas, J. Morales, and J. Khalife, "New-age satellite-based navigation – STAN: simultaneous tracking and navigation with LEO satellite signals," *Inside GNSS Magazine*, vol. 14, no. 4, pp. 56–65, 2019.

[22] Z. Kassas, J. Khalife, M. Neinavaie, and T. Mortlock, "Opportunity comes knocking: overcoming GPS vulnerabilities with other satellites' signals," *Inside Unmanned Systems Magazine*, pp. 30–35, June/July 2020.

[23] F. Farhangian and R. Landry, "Multi-constellation software-defined receiver for Doppler positioning with LEO satellites," *Sensors*, vol. 20, no. 20, pp. 5866–5883, October 2020.

[24] M. Orabi, J. Khalife, and Z. Kassas, "Opportunistic navigation with Doppler measurements from Iridium Next and Orbcomm LEO satellites," in *Proceedings of IEEE Aerospace Conference*, March 2021, accepted.

[25] J. Morales and Z. Kassas, "Tightly-coupled inertial navigation system with signals of opportunity aiding," *IEEE Transactions on Aerospace and Electronic Systems*, 2021, accepted.

[26] Z. Kassas, J. Khalife, K. Shamaei, and J. Morales, "I hear, therefore I know where I am: Compensating for GNSS limitations with cellular signals," *IEEE Signal Processing Magazine*, pp. 111–124, September 2017.

[27] K. Shamaei and Z. Kassas, "LTE receiver design and multipath analysis for navigation in urban environments," *NAVIGATION, Journal of the Institute of Navigation*, vol. 65, no. 4, pp. 655–675, December 2018.

[28] A. Abdallah and Z. Kassas, "Deep learning-aided spatial discrimination for multipath mitigation," in *Proceedings of IEEE/ION Position, Location, and Navigation Symposium*, April 2020, pp. 1324–1335.

[29] Z. Kassas, M. Maaref, J. Morales, J. Khalife, and K. Shamaei, "Robust vehicular localization and map matching in urban environments through IMU, GNSS, and cellular signals," *IEEE Intelligent Transportation Systems Magazine*, vol. 12, no. 3, pp. 36–52, June 2020.

[30] M. Maaref, J. Khalife, and Z. Kassas, "Lane-level localization and mapping in GNSS-challenged environments by fusing lidar data and cellular pseudoranges," *IEEE Transactions on Intelligent Vehicles*, vol. 4, no. 1, pp. 73–89, March 2019.

[31] M. Caamano, M. Felux, D. Gerbeth, J. Juan, G. Gonzalez-Casado, and J. Sanz, "Network-based ionospheric gradient monitoring to support GBAS," in *Proceedings of ION GNSS Conference*, 2019, pp. 2888–2902.

[32] M. Yoon, J. Lee, and S. Pullen, "Integrity risk evaluation of impact of ionospheric anomalies on GAST D GBAS," *NAVIGATION, Journal of the Institute of Navigation*, vol. 67, no. 2, pp. 223–234, 2020.

[33] E. Kaplan and C. Hegarty, *Understanding GPS: Principles and Applications*, 2nd ed. Artech House, 2005.

[34] J. Blanch, T. Walter, P. Enge, Y. Lee, B. Pervan, M. Rippl, and A. Spletter, "Advanced RAIM user algorithm description: Integrity support message processing, fault detection, exclusion, and protection level calculation," in *Proceedings of ION GNSS Conference*, September 2012, pp. 2828–2849.

[35] V. Kropp, "Advanced receiver autonomous integrity monitoring for aircraft guidance using GNSS," Ph.D. dissertation, University of Munich, Germany, 2018.

[36] J. Blanch, T. Walter, P. Enge, S. Wallner, F. Amarillo Fernandez, R. Dellago, R. Ioannides, I. F. Hernandez, B. Belabbas, A. Spletter *et al.*, "Critical elements for a multi-constellation advanced RAIM," *NAVIGATION, Journal of the Institute of Navigation*, vol. 60, no. 1, pp. 53–69, 2013.

[37] P. Roysdon and J. Farrell, "GPS-INS outlier detection and elimination using a sliding window filter," in *Proceedings of American Control Conference*, May 2017, pp. 1244–1249.

[38] S. Bhamidipati and G. Gao, "SLAM-based integrity monitoring using GPS and fish-eye camera," in *Proceedings of ION GNSS Conference*, September 2019, pp. 4116–4129.

[39] M. Maaref and Z. Kassas, "Measurement characterization and autonomous outlier detection and exclusion for ground vehicle navigation with cellular signals," *IEEE Transactions on Intelligent Vehicles*, vol. 5, no. 4, pp. 670–683, December 2020.

[40] M. Maaref and Z. Kassas, "Autonomous integrity monitoring for vehicular navigation with cellular signals of opportunity and an IMU," *IEEE Transactions on Intelligent Transportation Systems*, 2021, accepted.

[41] M. Maaref, J. Khalife, and Z. Kassas, "Enhanced safety of autonomous driving by incorporating terrestrial signals of opportunity," in *Proceedings of IEEE International Conference on Acoustics, Speech and Signal Processing*, May 2020, pp. 9185–9189.

[42] M. Maaref and Z. Kassas, "UAV integrity monitoring measure improvement using terrestrial signals of opportunity," in *Proceedings of ION GNSS Conference*, September 2019, pp. 3045–3056.

[43] K. Borre, D. Akos, N. Bertelsen, P. Rinder, and S. Jensen, *A Software-defined GPS and Galileo Receiver: A Single-frequency Approach*. Birkhäuser, 2007.

[44] T. Pany, *Navigation Signal Processing for GNSS Software Receivers*. Artech House, 2010.

[45] M. Braasch and A. Dempster, "Tutorial: GPS receiver architectures, front-end and baseband signal processing," *IEEE Aerospace and Electronic Systems Magazine*, vol. 34, no. 2, pp. 20–37, February 2019.

[46] J. del Peral-Rosado, J. Lopez-Salcedo, G. Seco-Granados, F. Zanier, P. Crosta, R. Ioannides, and M. Crisci, "Software-defined radio LTE positioning receiver towards future hybrid localization systems," in *Proceedings of International Communication Satellite Systems Conference*, October 2013, pp. 14–17.

[47] Z. Kassas and T. Humphreys, "Observability analysis of collaborative opportunistic navigation with pseudorange measurements," *IEEE Transactions on Intelligent Transportation Systems*, vol. 15, no. 1, pp. 260–273, February 2014.

[48] J. Khalife and Z. Kassas, "Precise UAV navigation with cellular carrier phase measurements," in *Proceedings of IEEE/ION Position, Location, and Navigation Symposium*, April 2018, pp. 978–989.

[49] S. Saab and Z. Kassas, "Power matching approach for GPS coverage extension," *IEEE Transactions on Intelligent Transportation Systems*, vol. 7, no. 2, pp. 156–166, June 2006.

[50] S. Aditya, H. Dhillon, A. Molisch, R. Buehrer, and H. Behairy, "Characterizing the impact of SNR heterogeneity on time-of-arrival-based localization outage probability," *IEEE Transactions on Wireless Communications*, vol. 18, no. 1, pp. 637–649, January 2019.